Real-time detection of turmeric adulteration with metanil yellow using a miniaturized NIR sensor and AI techniques

Dimitra Xenitopoulou [iD] *, Nikolaos L. Tsakiridis [iD], Achilleas Panagiotis Zalidis [iD]
George C. Zalidis [iD] *

Laboratory of Remote Sensing, Spectroscopy, and GIS, School of Agriculture, Aristotle University of Thessaloniki, Thessaloniki, 54124, Greece

ARTICLE INFO

ABSTRACT

Spices have been among the most targeted foods in the European Union (EU) for fraudsters, given that the spice market exemplifies complex and globalized supply chains. Turmeric is a widely used spice famous for its vivid color, flavor, and purported health advantages. Its medicinal properties in addressing various health issues have sparked a surge in global demand, raising concerns about the spice industry's integrity. The most common and hazardous adulterants of turmeric, added for financial gain, are synthetic, non-authorized azo dyes, particularly Metanil Yellow (MY). To tackle malpractices in the turmeric supply chain, this study proposes a scalable method utilizing a miniaturized near-infrared (NIR) (1350–2500 nm) sensor coupled with advanced Artificial Intelligence (AI) techniques to detect the presence of MY in turmeric. A dataset comprising 202 samples, including pure turmeric, MY, and their admixtures (5%–40% w/w), was analyzed using both the portable device and a high-resolution benchtop visible and near-infrared–short-wave infrared (VNIR–SWIR) spectroradiometer. Multiple spectral pre-treatments were applied, and classification was performed using Random Forest (RF), XGBoost, and Support Vector Machines (SVM). The best performance was achieved by the RF model on raw reflectance spectra collected with the miniaturized sensor (98% accuracy, $\kappa = 0.97$). Key diagnostic wavelengths (e.g., 1495, 1640, 1675, 2155, 2475 nm) linked to MY's chemical structure were pinpointed through feature importance analysis. This work highlights the potential of portable, low-cost NIR sensors as tools for broadening access to food authentication, enabling rapid, non-destructive testing with a practical limit of detection of 5% w/w for MY adulteration.

1. Introduction

The worldwide demand for spices and herbs has been increasing, driven by their expanding role in the food service sector, e.g., as additives in ready-made meals, the modern consumer's quest for unfamiliar flavors and ethnic dishes, and their perceived health benefits (Bhatkar et al., 2023). The supply chains in the spice and herb sector are typically lengthy and complex, involving multiple countries. Europe, with its unsuitable climate for most spice plants, imports hundreds of thousands of tons of spices annually, primarily from East Asia. Intra-EU spice trade mainly involves re-exports of spices initially imported from outside the EU. In many non-EU countries, spices and herbs are cultivated on a subsistence level, with numerous intermediaries in the supply chain, creating opportunities for malpractice and fraud, some posing serious health risks (e.g., using unauthorized dyes for color enhancement) (Maquet et al., 2021).

Turmeric (*Curcuma longa* L.) powder, also known as ground turmeric, is one of the most commonly used spices in the food industry, mainly as a natural coloring agent due to its content of various carotenoid compounds responsible for its yellowish color (Mukherjee et al., 2009). Among the various phytochemical compounds present in turmeric, curcumin ($C_{21}H_{20}O_6$), present in up to 5%, is its main bioactive compound (Nelson et al., 2017), having diverse applications in the pharmaceutical, food, and cosmetic industries (Rukundo and Danao, 2020). Historically used as a natural medicine in Asia, turmeric is extensively studied today for its beneficial effects on human health (El-Saadony et al., 2023; Singletary, 2020; Abd El-Hack et al., 2021). Its use also improves food products' nutritional, technological, and organoleptic properties (Sharifi-Rad et al., 2020).

Given its importance, turmeric has become widely popular in the market. The increased interest in this product, combined with the complexity of its supply chain, has led to its regular adulteration with economic incentives. **Metanil Yellow (MY)**, a non-permitted synthetic dye, is the most common adulterant, along with others such as starch, chalk powder, and lead chromate (Rukundo et al., 2020).

MY (C$_{18}$H$_{14}$N$_3$NaO$_3$S), also referred to as **Acid Yellow 36**, is a water-soluble azo dye with a color index of 13.065 (Rukundo et al., 2020), relatively low cost, high degradation stability, and readily available (Khan et al., 2020). It can mimic curcumin's appearance and be mixed with turmeric up to 50% w/w without altering turmeric's organoleptic properties such as aroma (Dhakal et al., 2016). Numerous studies report MY adulteration (Dixit et al., 2008, 2009; Nath et al., 2015; Kaur Purba and Sudhir K. Shukla, 2015; Jaiswal et al., 2016; Verma et al., 2022; Phukan et al., 2022), with most of them involving turmeric samples originating from Asia, particularly India. Frequent MY intake poses health risks, including serious effects on the nervous and gastrointestinal systems, and is linked to methaemoglobinaemia, cyanosis, allergic dermatitis, and carcinogenicity (Sundaresan and Vijaikanth, 2024). According to the 2005 opinion of the European Food Safety Authority (EFSA) (EFSA Panel on Food Additives, Flavourings, Processing Aids and Materials in Contact with Food (AFC), 2005), MY is included in a group of pigments that should be considered genotoxic and/or carcinogenic. More extensive reports on the harmful health effects of MY are available in the literature (Khan et al., 2020; Tawfeek et al., 2021; Islam et al., 2023; Kamali et al., 2023).

Controlling the presence of non-authorized dyes, such as MY, is imperative to protect public health and ensure food quality. Various laboratory-based methods have been developed to detect MY in ground turmeric, including chromatographic methods (Bonan et al., 2013; Ashok et al., 2015; Nath et al., 2015; Arabkhani et al., 2022). However, these methods are time-consuming, involve complex (pre-)processing protocols for samples, require skilled personnel and are limited to lab settings while the equipment, consumables, and chemical reagents they rely on are often quite expensive (Rukundo and Danao, 2020; Ranjan et al., 2021). In contrast, **near-infrared spectroscopy (NIRS)** offers a non-destructive, rapid, cost-effective, and more environmentally friendly alternative, as it eliminates the need for chemical reagents and sample disposal associated with conventional methods (Buthelezi et al., 2019). Once a food sample is analyzed using NIRS, the vibrational spectrum behaves as the so-called "fingerprint" of the sample, allowing researchers to quantify, qualify, characterize, and elucidate the intrinsic properties of food ingredients and products (Cozzolino, 2022). The rise in the production and development of miniaturized near-infrared (NIR) spectrometers in recent years has increased their availability and reduced their purchase costs (Beć et al., 2022), thus enabling their acquisition and use by a larger proportion of people. Such portable NIR sensor systems allow real-time and non-destructive monitoring of the integrity of food products at every stage of their supply chain, making it a promising tool for producers, inspection agencies, certification bodies, distributors, retailers, and perhaps later on for consumers themselves.

NIR spectroscopy offers many advantages, but one of its key limitations is the vast amount of data it generates. Extracting important information from this data is crucial for optimal results (Teixeira and Sousa, 2019). Artificial Intelligence (AI)-based methods such as machine learning (ML) are capable tools to gain a deeper understanding of the data (Houhou and Bocklitz, 2021). By using these tools, analysts are able to isolate and interpret information from complex datasets, visualize patterns within the data, and create mathematical connections between different data sources (e.g., calibration and validation models) (Szymańska et al., 2015; Szymańska, 2018; Sultanbawa et al., 2021). According to Rukundo and Danao (2020), when NIR spectral data are combined with multivariate analytical techniques, such as principal component analysis (PCA), partial least squares regression (PLSR), soft independent modeling by class analogy (SIMCA), or discriminant analysis, they become meaningful.

Limited work has been conducted over the last decade on the determination of MY in turmeric using handheld NIR instruments (Kar et al., 2017; Rukundo et al., 2020; Rukundo and Danao, 2020). In fact, the number of miniaturized sensors examined in these studies is even more limited, despite the strong increase in their availability and the variety of corresponding instruments on the market. To the best of our knowledge, (Rukundo and Danao, 2020) successfully used the ASD QualitySpec Trek handheld spectrometer (Malvern Panalytical, Longmont, CO) to detect the source of turmeric using both unadulterated and MY-adulterated samples, using Savitzky–Golay (SG) smoothing and PCA-SIMCA models. The same device was also used in Rukundo et al. (2020), comparing its performance in predicting MY concentration (0%–30% w/w) with that of a benchtop laboratory NIR instrument. Results showed that the portable sensor, combined with pre-processing techniques such as standard normal variate (SNV) and PLSR model development, produced reliable results, making it suitable for cost-effective screening and real-time authentication of ground turmeric. Kar et al. (2017) used a miniaturized NIR spectrometer from StellarNet Inc. (USA) to detect and quantify MY in turmeric powder. Principal component regression (PCR) and PLSR models predicted MY concentrations from 1%–25% w/w, with PLSR performing better. Significant absorption peaks related to MY were identified in the 1000–1200 nm and 1350–1550 nm regions. Although the literature supports the effectiveness of portable NIR instruments for MY detection in turmeric, it remains limited in both the number of studies and the diversity of sensors investigated.

The present study evaluates the capability of a new **miniaturized Fourier Transform (FT) NIR device (1350–2500 nm)**, the NeoSpectra Scanner (Si-Ware Systems), paired with AI techniques to identify turmeric adulteration with the non-authorized dye MY at adulteration levels between 5% and 40% w/w. This concentration range was selected as it reflects realistic economically motivated fraud scenarios and matches the detection capabilities of portable NIR devices under field conditions. The spectrometer used in this work is about three times cheaper than the DWARF-Star Miniature NIR Spectrometer (StellarNet Inc.) and more than ten times cheaper than the ASD QualitySpec Trek (Malvern Panalytical). While the ASD model offers a broad spectral range (350–2500 nm) with specific spectral resolutions at various wavelengths, it is very expensive, heavy, and massive, making it less convenient for frequent on-site testing. On the other hand, the DWARF-Star provides high spectral resolution (down to 1.25 nm), is compact and durable, and is more affordable, but it requires an external power source and covers a narrower NIR range (900–1700 nm). To put our results in perspective, we compare our findings using a more detailed but more costly visible and near-infrared (VNIR) – short-wave infrared (SWIR) [VNIR–SWIR] spectrometer (350–2500 nm) in terms of detection capability (i.e., AI model performance). The proposed approach represents a promising non-destructive and environmentally friendly solution for on-site testing of turmeric authenticity at various supply chain stages, enhancing transparency and accountability in the spice industry and strengthening consumer trust. Importantly, our methodology also highlights specific diagnostic wavelengths that serve as robust spectral indicators of MY adulteration, knowledge that can support the design of next-generation sensors tailored for targeted, low-cost, and rapid fraud detection in the field.

2. Materials and methods

2.1. Dataset formulation

The overall methodological approach is illustrated in Fig. 1. It is comprised of two parts: (i) data acquisition, where the samples (i.e., pure, adulterant, and adulterated) are prepared in pre-determined adulteration levels, and their spectral diffuse reflectance recorded, and (ii) data analysis where the AI-driven chemometrics models infer the adulteration level based purely on the recorded spectra.
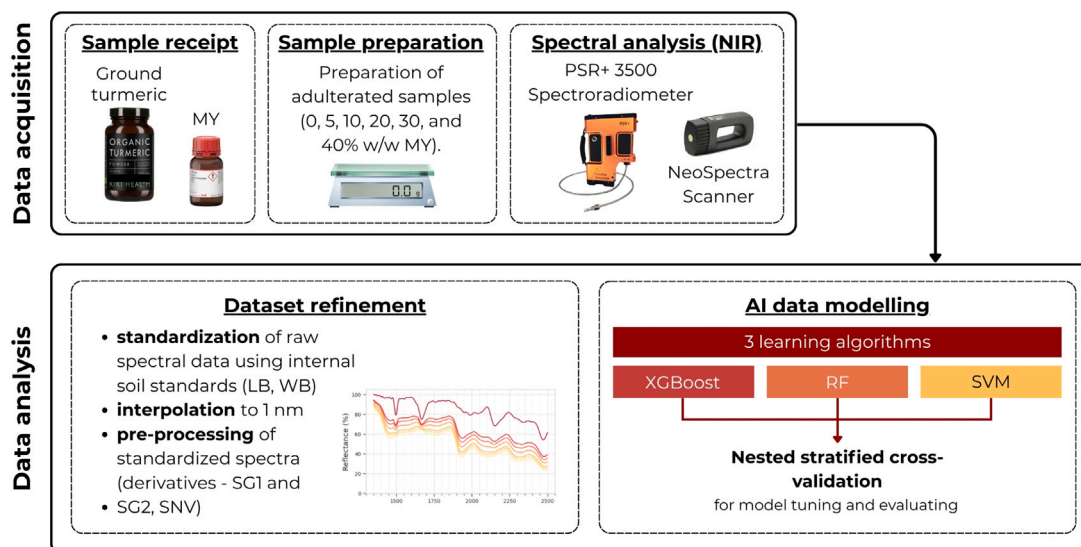
Fig. 1. Flowchart of the methodological process adopted in the current work for the spectral analysis of turmeric adulteration.

2.1.1. Collection of samples

Fifty (50) pure samples of certified 100% organic ground turmeric (KIKI Ltd., United Kingdom), originating from ten (10) different bottles (packages) of this product with five (5) different LOT numbers, and sixteen (16) pure samples of MY in powder form (Tokyo Chemical Industry Co., Ltd., Japan) were collected. The turmeric product is certified organic by the UK Soil Association, a recognized third-party body that ensures compliance with established organic farming and processing standards applicable in the United Kingdom (UK) and aligned with European regulations. The spectral measurements of the pure samples were carried out directly after opening their packages.

2.1.2. Preparation of adulterated samples

The adulterated samples (20 g each) were prepared by mixing pure turmeric with MY at five (5) distinct weight-to-weight (w/w) adulteration levels: 5%, 10%, 20%, 30%, and 40%. Specifically, for each adulteration level, appropriate quantities of turmeric and MY were weighed on an analytical balance (METTLER TOLEDO, USA) as follows: 19 g turmeric + 1 g MY (5%), 18 g turmeric + 2 g MY (10%), 16 g turmeric + 4 g MY (20%), 14 g turmeric + 6 g MY (30%), and 12 g turmeric + 8 g MY (40%). These mixtures were prepared from a randomly selected subset of 14 pure turmeric samples, resulting in a total of seventy (70) adulterated samples. Mixing was carried out manually using a 150 mm grooved spatula made of 304-grade stainless steel for approximately one (1) minute, ensuring homogeneous distribution of MY in the turmeric powder. The powders were mixed inside 400 mL polypropylene laboratory beakers with a pouring spout, and the resulting blends were transferred into semi-transparent polypropylene containers with screw caps for safe storage and light shielding. To confirm sample homogeneity, spectral measurements of the adulterated samples were obtained immediately after their creation.

2.1.3. Spectral data acquisition and standardization

The reflectance spectra of all samples (i.e., 100 pure turmeric and 32 MY samples and their 70 admixtures, a total of 202 samples, 20 g each) were collected using a portable NIR spectrometer and a benchtop VNIR–SWIR spectrometer, as described below. The benchtop VNIR–SWIR spectrometer was used as a high-precision benchmark to validate the accuracy and reliability of the portable NIR spectrometer. In both cases, the raw spectral data were further standardized based on the spectral signatures of internal soil standards (Lucky Bay – LB and Wylie Bay – WB).

NIR-diffuse reflectance spectra (1350–2500 nm with a resolution of 16 nm at $\lambda = 1,550$ nm) were collected with a **handheld FT-NIR spectrometer**, the **NeoSpectra Scanner** (Si-Ware Systems, Menlo Park, CA, USA) (Fig. 2a), equipped with the NeoSpectra powder sample kit (Si-Ware Systems, Menlo Park, CA, USA). The dimensions of the device are $178 \times 91 \times 62$ mm with a weight of 1 kg. The spectral analysis involved placing the samples on a small flat-bottom 30 mm soda-lime glass dish that fits into a holder (power cup adapter) on top of the scanner. To ensure consistent compaction and improve spectral signal quality, a small metal weight (plumb) included in the kit was placed on top of the sample, following the manufacturer's instructions. As a reference, a ceramic reflection reference tile, with almost flat spectral response in NIR, that is included in the kit, was used. This reflection standard was placed in the empty glass dish before each use to calibrate the device, following the manufacturer's measurement protocol. The calibration was performed approximately ten (10) minutes after the spectrometer was turned on, and it was repeated after every set of five (5) samples scanned. Each sample was scanned two (2) times and then these two recorded spectra were averaged for the analysis. During each calibration, a spectral signature of the white reference material used for calibration was also recorded, followed by the measurements of the internal soil standards (LB and WB). The device settings during the measurements were as follows: a 5 s scan time, a default optical gain, and linear interpolation set to 257 points and saved as wavenumbers (cm^{-1}). The acquisition method was carried out via a proprietary application – NeoSpectra Collect ™ © 2021 SWS (app version: 7.1.230328) that was installed on a mobile device and was connected to the sensor wirelessly via BlueTooth. Data was saved on the mobile device in the app's default format and was later exported as .csv files and transferred to a desktop computer for further processing.

Concerning the VNIR–SWIR spectrum, spectral acquisitions were performed using the **PSR+ 3500 Spectroradiometer** (Spectral Evolution Inc., Lawrence, MA, USA), with a contact probe spectrometer that covers the wavelength range of 350–2500 nm (Fig. 2b). As described by Kalopesa et al. (2023), the spectrometer employs a 512-element Si photodiode array to cover the 350–1000 nm range, offering a full width at half maximum (FWHM) resolution of 2.8 nm at 700 nm. For the 970–1910 nm range, it uses a 256-element InGaAs detector with a FWHM resolution of 8 nm at 1500 nm, and another 256-element InGaAs photodiode array for the 1900–2500 nm range, delivering a FWHM resolution of 6 nm at 2100 nm. The final data output is provided in 1 nm resolution (i.e., 2151 bands from 350 nm to 2500 nm inclusive). To capture the spectrum, the spectrometer's contact probe
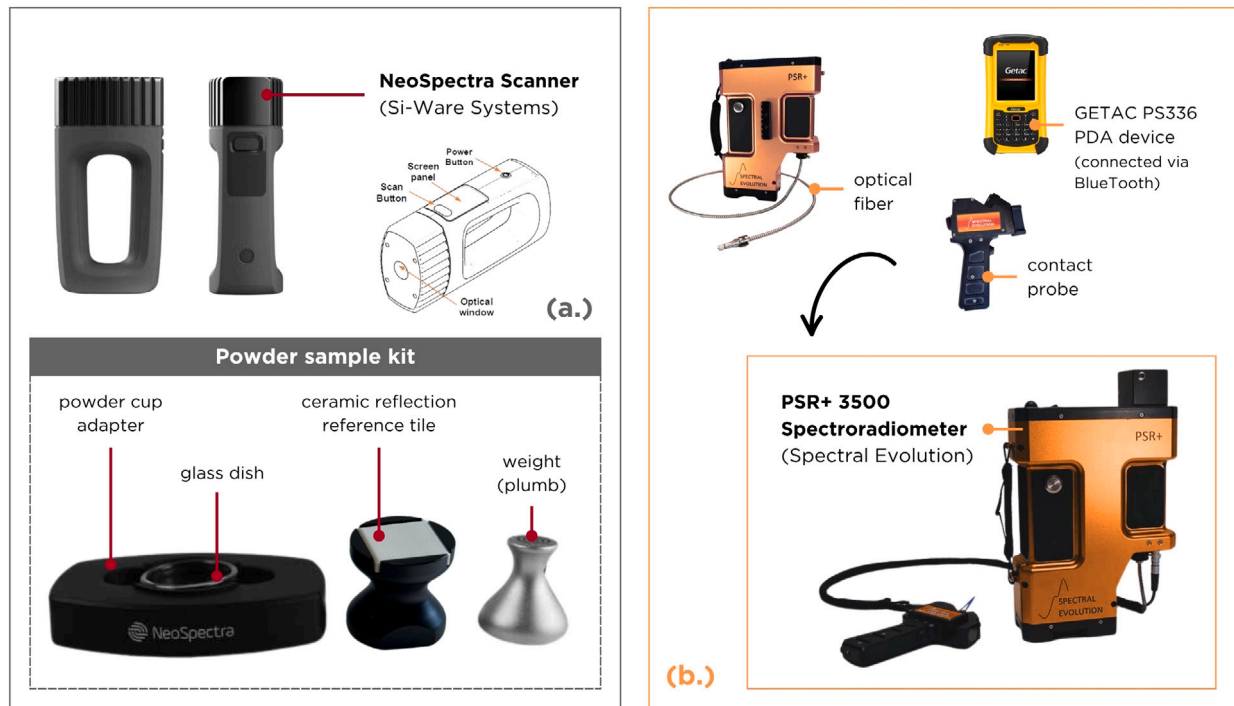
Fig. 2. Sensors used in the study — instrumentation. (a) The NeoSpectra Scanner (Si-Ware Systems) and its powder sample kit, used to collect reflectance spectra of powdered samples in a portable setup. (b.) High-resolution spectroradiometer system used as a reference instrument for benchmarking the performance of the portable NIR device.

was placed directly on top the powder. The spectra were recorded in reflectance mode, with each measurement representing the average of three (3) scans. Calibration was performed using a standard Spectralon® white reference material and was repeated after every 10 samples to maintain sensor accuracy and precision. As in the case of the NeoSpectra Scanner, each calibration was followed by the corresponding measurement of the white reference material as well as the internal soil standards. The acquisition method was operated by the proprietary application DARWin™ SP Data Acquisition Software (app version: v.1.2.5842) that was installed on a GETAC PS336 PDA device that connected wirelessly over Bluetooth to the spectrometer. Data was autosaved as text (.sed format) and binary formats (.raw format) on the PDA device. Then the data was transferred to a desktop computer for further processing through an internal script developed, including the conversion of the measurements to a .csv file.

Employing internal soil standards such as LB and WB is crucial for maintaining consistency and comparability of spectral measurements conducted by different spectroscopic devices. As two spectrometers were used in the current study, standardization helped minimize instrument-specific differences in order to make spectral comparisons direct. According to Ben Dor et al. (2015), soil standards that are well-defined serve as dependable reference materials that improve the reproducibility of spectral data and calibrations. Beyond strengthening the current analysis, this process ensures that the spectral data produced in this work can be effectively compared with other studies and data sets, making it easier to integrate results across different spectroscopic systems.

2.1.4. Processing of the data

As the NeoSpectra Scanner provided the spectral data recorded in wavenumbers (cm^{-1}), these were then converted to wavelengths (nm) for consistency with the spectral data obtained from the PSR+ 3500 Spectroradiometer. This transformation was performed using the following conversion formula:

$$\lambda = \frac{10^7}{\tilde{\nu}} \tag{1}$$

where λ is the wavelength in nm, and $\tilde{\nu}$ is the wavenumber in cm^{-1}.

Following this transformation, the spectra were interpolated to a 1 nm resolution using piecewise linear interpolation to harmonize the data structure across both instruments. This step guaranteed direct comparability between the datasets, facilitating robust data analysis and model development.

2.2. Analysis using Artificial Intelligence

2.2.1. Spectral pre-treatments

Spectral pre-treatments are crucial for enhancing the quality of spectral data by removing noise, correcting baseline shifts, or emphasizing specific spectral features (Rinnan et al., 2009). In this study, several pre-treatment methods were applied to the initial reflectance spectra and the pseudo-absorbance spectra, derived by applying the logarithmic transformation to the inverse of the reflectance: (i) the baseline Reflectance data were used without any transformation; (ii) the Reflectance + SNV treatment applied the SNV to correct for scatter effects by centering and scaling each spectrum; (iii) the SG filter was utilized for smoothing and derivative computation, including first-derivative smoothing of the absorbance (Abs-SG1) with a window length of 31 data points (corresponding to 31 nm) and a third-order polynomial, (iv) Abs-SG1 but with a larger window length of 51 data points (i.e., 51 nm), (v) Abs-SG2, i.e., second-derivative smoothing with a window length of 31 data points (corresponding to 31 nm) and a third-order polynomial, and (vi) Abs-SG2 but with a larger window length of 51 data points (i.e., 51 nm).

It should be noted that, following the application of spectral pre-treatments and prior to inputting the data into the learning algorithms, the spectra were resampled to a resolution of 5 nm in order to mitigate multicollinearity and better approximate the true spectral resolution of the instruments.

2.2.2. Learning algorithms considered

The **Random Forest (RF)** classifier is an ensemble learning algorithm that generates multiple decision trees during training and determines the final class by aggregating their predictions, typically using majority voting (Breiman, 2001). Each tree is built using a subset of the data sampled with replacement (bootstrap sampling) and a random subset of features for splitting at each node, enhancing model diversity. Key hyperparameters include the number of trees, $n_{\text{estimators}}$, which controls the size of the ensemble and the maximum depth of each tree, which determines the complexity of individual trees. Other critical hyperparameters are the minimum number of samples required to split a node and the minimum number of samples per leaf. By combining the predictions of diverse trees, RF mitigates overfitting and improves generalization, making it robust against noisy data.

The **XGBoost** classifier, based on gradient-boosted decision trees, optimizes the prediction by sequentially adding trees to minimize a specified loss function (Chen and Guestrin, 2016). Unlike RF that uses bootstrapping, XGBoost uses a boosting approach, where each tree corrects the errors of its predecessors, leveraging second-order gradients for efficient optimization. The primary hyperparameters include the number of boosting rounds, $n_{\text{estimators}}$, and the learning rate, η, which controls the contribution of each tree. The maximum depth of trees regulates model complexity, while the regularization terms λ (L2) and α (L1) in the objective function reduce overfitting. Additionally, the subsampling ratio and the column sampling ratio enhance generalization by introducing randomness in tree building. XGBoost's scalability and advanced optimization techniques make it particularly effective for tabular data.

The **Support Vector Machine (SVM)** classifier is a kernel-based learning algorithm that finds an optimal hyperplane to separate data points in a high-dimensional space (Cortes and Vapnik, 1995). By maximizing the margin between classes, SVM ensures robust generalization. The effectiveness of SVM largely depends on the choice of the kernel function, with common options being the linear and radial basis function (RBF) kernels. Key hyperparameters include the regularization parameter, C, which controls the trade-off between maximizing the margin and minimizing classification errors, and the kernel coefficient, γ, which influences the decision boundary for non-linear kernels. A higher γ results in more complex decision boundaries, potentially leading to overfitting, whereas a lower γ produces smoother, more generalized models. SVM is particularly effective in high-dimensional spaces and is less prone to overfitting when properly tuned.

2.2.3. Splitting of the dataset and hyperparameter tuning

To ensure robust model evaluation and optimal hyperparameter selection, we employ a **nested cross-validation** approach (Algorithm 1). This method consists of an *outer loop*, responsible for assessing model generalization, and an *inner loop*, dedicated to hyperparameter tuning. Specifically, we use a 5-fold outer cross-validation, where the dataset is split into five disjoint subsets. For each iteration, four subsets are used for training, and the remaining one serves as the test set. Within each training fold, an internal 5-fold cross-validation is performed to optimize hyperparameters.

For each model, we perform an exhaustive grid search within the inner loop to identify the best hyperparameter configuration based on classification accuracy. The optimal model is then evaluated on the unseen test fold from the outer loop. This process is repeated five times, ensuring that each sample is used once as a test set. By using nested cross-validation, we mitigate the risk of overfitting and obtain an unbiased estimate of model performance. Specifically, we considered the following parameters:

- **Random Forest**: $n_{\text{estimators}}$ = {50, 100, 200}, maximum depth of tree = {None, 10, 20}

- **XGBoost**: $n_{\text{estimators}}$ = {50, 100, 200}, η = {0.01, 0.05, 0.1}, maximum depth of trees = {3, 6, 9}, λ = {0, 0.1, 1, 5}, α = {0, 0.1, 1, 5}, subsampling ratio = {0.7, 1.0}, column sampling ratio = {0.7, 1.0}.

- **Support Vector Machine**: C = {0.01, 0.1, 1, 10, 100}, kernel = {linear, RBF, polynomial, sigmoid}, γ = {1 / ($n_{\text{features}} \cdot \text{Var}(X)$), 1 / n_{features}, 0.001, 0.01, 0.1, 1}

Additionally, **out-of-fold (OOF) predictions** are collected during the inner loop, allowing us to analyze model consistency and stability. The final evaluation metrics are averaged across all outer folds to provide a comprehensive assessment of classifier performance.

Algorithm 1 Nested Cross-Validation with Out-of-Fold Predictions

---

1: **procedure** NESTEDCV(Dataset D, outer folds $k_{\text{outer}} \in \mathbb{N}^+$, inner folds $k_{\text{inner}} \in \mathbb{N}^+$, hyperparameter set H)
2:     $D_{\text{outer}} \leftarrow$ SPLITFOLDS(D, k_{outer})
3:     Initialize list of out-of-fold predictions $P_{\text{outer}} \leftarrow []$
4:     **for** each outer fold $i = 1, \ldots, k_{\text{outer}}$ **do**
5:         $D_{\text{test}} \leftarrow D_{\text{outer}}[i]$
6:         $D_{\text{train}} \leftarrow D \setminus D_{\text{test}}$
7:         Initialize: best hyperparameters $h^* \leftarrow \varnothing$, best score $s^* \leftarrow -\infty$
    ▷ (or use ∞ for error minimization)
8:         $D_{\text{inner}} \leftarrow$ SPLITFOLDS($D_{\text{train}}, k_{\text{inner}}$)
9:         **for** each hyperparameter configuration $h \in H$ **do**
10:             Initialize list of inner scores $P_{\text{inner}} \leftarrow []$
11:             **for** each inner fold $j = 1, \ldots, k_{\text{inner}}$ **do**
12:                 $D_{\text{val}} \leftarrow D_{\text{inner}}[j]$
13:                 $D'_{\text{train}} \leftarrow D_{\text{train}} \setminus D_{\text{val}}$
14:                 Train model M with configuration h on D'_{train}
15:                 $p \leftarrow$ EVALUATE(M, D_{val})
16:                 Append p to P_{inner}
17:             $s \leftarrow$ AVERAGE(P_{inner})
18:             **if** $s > s^*$ **then**   ▷ (or less than for minimization)
19:                 $s^* \leftarrow s$
20:                 $h^* \leftarrow h$
21:         Train final model M^* on D_{train} with hyperparameters h^*
22:         $s_i \leftarrow$ EVALUATE(M^*, D_{test})
23:         $p_{\text{test}} \leftarrow$ PREDICT(M^*, D_{test})
24:         Append p_{test} to P_{outer}
25:     **return** $\{s_i\}_{i=1}^{k_{\text{outer}}}$, P_{outer} ▷ Return outer fold scores & predictions

---

2.2.4. Model evaluation metrics

To evaluate the models, we used a comprehensive set of metrics: **accuracy, Cohen's kappa** (κ)**, precision, recall, and F1-score** (Hastie et al., 2009). Accuracy, a straightforward and widely used measure, calculates the proportion of correctly classified instances out of the total instances, providing an overall assessment of model performance. However, accuracy alone may not fully reflect model efficacy, particularly in cases of class imbalance, as it does not account for agreement by chance. To address this limitation, we also employed Cohen's kappa, a metric that adjusts for the probability of chance agreement between predicted and actual classifications. Cohen's kappa ranges from -1 to 1, where values close to 1 indicate strong agreement, values near 0 suggest random-level agreement, and negative values imply worse-than-random performance.

In addition, we report **precision**, **recall**, and the **F1-score**, averaged using the *weighted* method across the five cross-validation folds. These metrics are particularly informative in imbalanced datasets, such as ours, where the majority class comprises pure samples and minority classes are underrepresented. Precision measures the proportion of true positives among all predicted positives, recall indicates the proportion of true positives among all actual positives, and the F1-score represents their harmonic mean. The use of weighted averaging (i.e., which calculates metrics for each label, and find their average
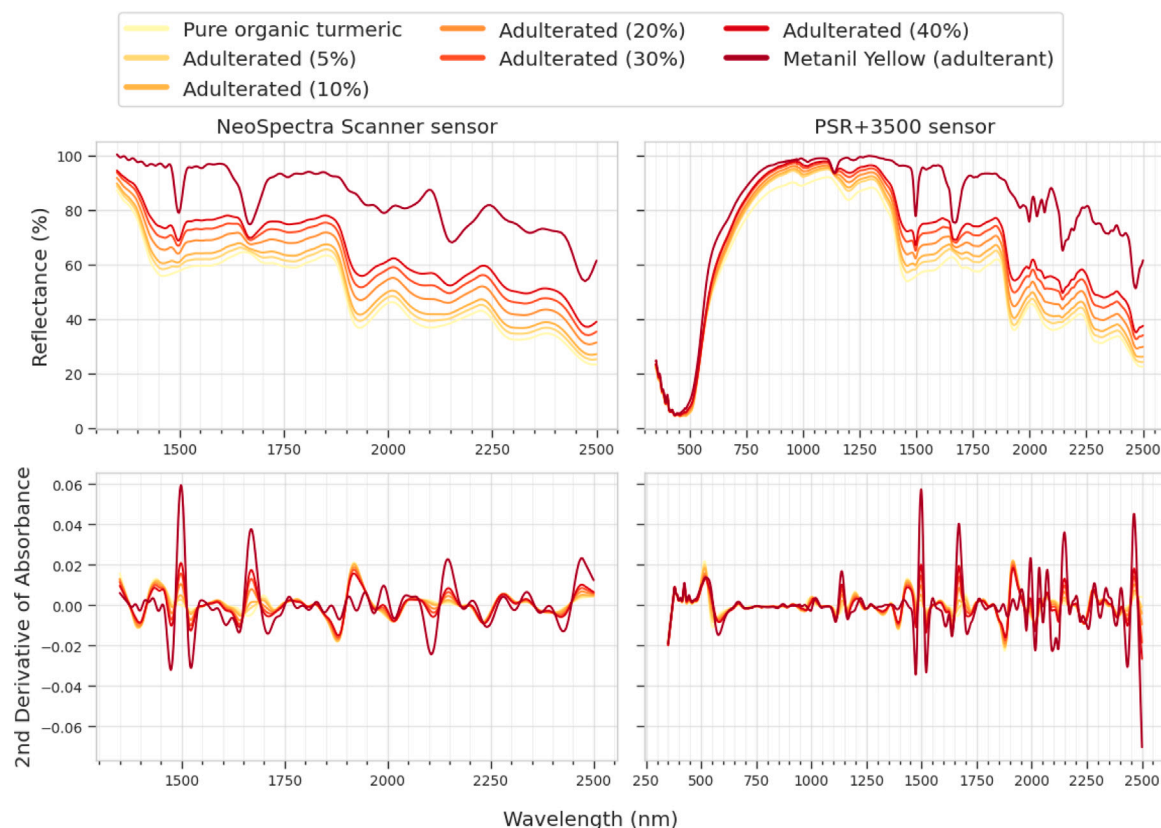
Fig. 3. The effect of the adulteration level on the mean reflectance spectra (top row) and the second derivative of absorbance (bottom row) of both sensors.

weighted by support — the number of true instances for each label) ensures that the contribution of each class to the final score reflects its relative frequency, offering a more realistic and balanced view of model performance. By considering all five metrics with appropriate averaging, we provide a more robust and comprehensive evaluation of classification reliability under class imbalance.

3. Results and discussion

3.1. Qualitative analysis of the spectra

3.1.1. Reflectance spectra analysis

The infrared reflectance spectra of pure turmeric, pure MY, and their adulterated mixtures were obtained using both the NeoSpectra Scanner (left) and the PSR+ 3500 Spectroradiometer (right) and they are presented in Fig. 3. As expected, increasing levels of MY adulteration resulted in systematic alterations in the spectral profiles. More specifically, a significant increase in albedo is evident in the adulterated samples, attributed to the higher inherent reflectance of MY compared to pure turmeric. In addition, as the adulteration level increases, certain absorption bands where MY exhibits distinct spectral features (e.g., at approximately 1500 nm, 1660 nm, 2150 nm, and 2460 nm) become more pronounced in the adulterated spectra, indicating a direct correlation between adulteration level and spectral response.

These results are consistent with previous findings on MY absorption characteristics (Rukundo et al., 2020), which indicate that in the spectral regions near 1480–1680 nm, 1740 nm, and 2470 nm, differences in the chemical composition of MY compared to pure turmeric are distinct. In particular, it is noted that these wavelengths are associated with vibrational modes of –NH, –SH bonds, which are not present in the turmeric compound. According to Dhakal et al. (2016), MY carries three nitrogen atoms (N=N and –NH) and one sulfate group ($SO_3{}^{2-}$), while it lacks a methyl group ($-CH_3$) and oxygens other than those included in the corresponding sulfate group.

The aforementioned findings are further supported and complemented by the work of Kar et al. (2017), who highlight that the spectral regions from 1000 nm to 1200 nm and from 1350 nm to 1550 nm correspond to the second overtone region of N–H bonds and the first overtone region of the same bonds, respectively. Although wavelengths below 1350 nm are beyond the detection capabilities of the NeoSpectra Scanner, the spectral signatures obtained using the PSR+ 3500 reveal a distinct peak around 1150 nm, which is attributed to MY. However, this peak does not appear to significantly influence the absorbance profile of the adulterated samples, in contrast to the more pronounced effects observed in the regions discussed earlier.

In addition to the distinctive peaks attributed to MY, spectral regions characteristic of pure turmeric, particularly the absorption bands around 1450 nm and 1930 nm, can also help differentiate the two substances. These bands are primarily associated with O–H bonds, typically arising from moisture (water) content, especially in dry foods, such as powders. In general, water's strong NIR absorption bands at 1400–1440 nm and 1900–1950 nm have frequently been used to quantify the amount of water in foods (Büning-Pfaue, 2003). As a synthetic dye designed for stability and color Intensity, MY has no hydroxyl groups and bound water, uses sulfonic acid groups ($-SO_3H$) instead to improve solubility in aqueous environments, and thus does not exhibit these specific absorption features.

By applying the second Savitzky–Golay derivative (SG2) to the standardized and interpolated absorbance data shown in the bottom section of Fig. 3, the spectral absorption peaks become more pronounced, facilitating their identification. The pure MY spectrum (depicted in dark red) exhibits strong absorption features at particular positions distinct from those of pure turmeric (light yellow to beige), offering more diagnostic information than the initial data, especially in the case of the NeoSpectra Scanner. It is worth noting that in the PSR+ 3500 data, considerable noise appears beyond 1900 nm. Differences among the various adulteration levels become more discernible following the
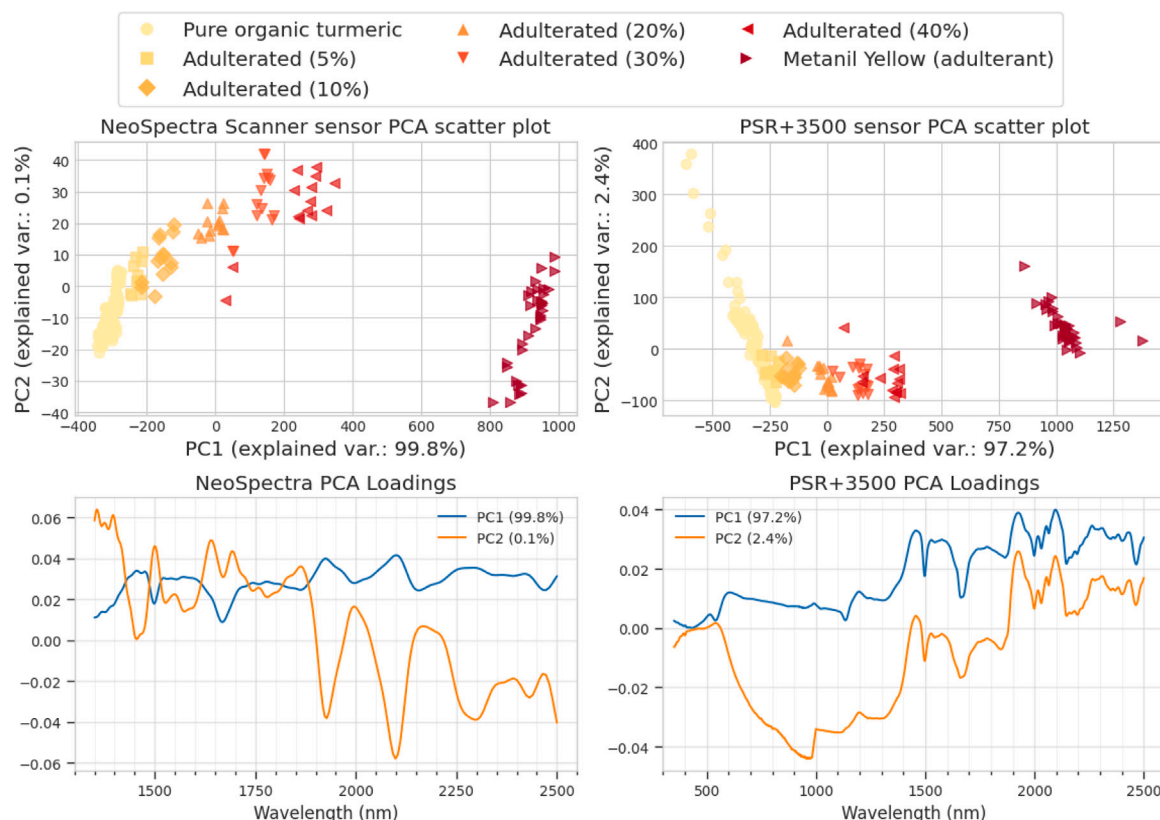
Fig. 4. The effect of the adulteration level on the reflectance spectra of both sensors, as shown in the PC space; PCA scatter plot (top row) and loadings (bottom row). The explained variance of each PC is shown in parentheses.

application of SG2, particularly in the data acquired using the portable spectrometer compared to the reference instrument. The broader spectral range of the latter allows exploration of regions containing more informative features for differentiating the two compounds. As observed in the PSR+ 3500 Spectroradiometer's plot, the most relevant spectral information for detecting the presence of MY in turmeric lies above 1250 nm.

3.1.2. PCA of reflectance spectra from both sensors

The effect of the presence of the MY on the reflectance spectra was further explored using PCA, which was applied separately to the spectral datasets acquired from the NeoSpectra Scanner (left panel) and the PSR+ 3500 benchtop sensor (right panel), as depicted in Fig. 4.

In both cases PCA revealed a fairly clear distinction between pure turmeric, adulterated samples and MY. According to the two plots (Fig. 4, top row), there appears to be a common pattern in spectral differentiation, with pure turmeric samples (yellow-beige markers) clustered relatively closely at the lower end of PC1, indicating high spectral consistency, particularly in the case of the NeoSpectra Scanner. As the level of adulteration increases, the adulterated samples (orange to red markers) are progressively shifted towards the positive axis of PC1, reflecting systematic changes in spectral properties due to contamination. Concerning the low-level adulteration (5%–10%), partial overlap with the pure turmeric samples is observed, whereas higher adulteration levels (≥20%) progressively diverge from the pure turmeric cluster, forming more distinctly defined groups. Similar findings were reported by Kar et al. (2017), who also employed NIR spectroscopy to detect the presence of MY in turmeric powder. Their results indicated that PCA-based clustering became more pronounced at higher concentrations of the adulterant, while lower-level adulterated samples showed greater overlap with the authentic ones. This suggests a direct relationship between the degree of spectral differentiation and the MY content in turmeric, a trend that aligns closely with the observations of the present

study. It is further noted that, as with pure turmeric, MY (dark red markers) forms a distinct cluster, clearly distant from that of turmeric, thus reinforcing the spectral uniqueness of MY compared to that of this spice and highlighting the potential of PCA in distinguishing between pure and adulterated samples. The corresponding PCA loadings plots (Fig. 4, bottom row) indicate that the most influential wavelengths for class separation are those with the highest absolute loading values. For the NeoSpectra sensor, notable peaks occur slightly below 1500 nm, around 1660 nm, approximately at 1920 nm, and just above 2100 nm, while for the PSR+ 3500, larger contributions are observed near 1000–1200 nm, 1450–1650 nm, and 1900–2100 nm.

Although both sensors enabled differentiation between pure and adulterated turmeric samples within the PCA space, a closer examination reveals that the PCA derived from NeoSpectra data results in more distinctly separated clusters compared to the PCA based on PSR+ 3500 spectra. While the PSR+ 3500 benefits from broader spectral coverage and higher resolution, it also introduces a significantly larger number of variables (wavelengths), many of which may be redundant or irrelevant in terms of detecting the adulterant. As a result, the PCA applied to the PSR+ 3500 spectra must compress a more complex, high-dimensional dataset into just two principal components (PC1 and PC2), potentially leading to less apparent separation among classes in the projected space. The earlier observation that the spectral region between 350 nm and 1250 nm—covered only by the PSR+ 3500 and not by the NeoSpectra Scanner—does not appear to carry significant discriminative information, may provide a reasonable explanation for the superior performance of the NeoSpectra in this specific multivariate analysis.

3.2. AI model analysis

3.2.1. Model accuracy

Table 1 summarizes the mean classification accuracy and Cohen's κ across the five outer folds for each combination of learning algorithm,

spectral pre-treatment method, and sensor type. Overall, the RF classifier achieved the highest performance across both sensors, particularly when applied to absorbance spectra smoothed using either the SG1 or SG2 filters with a window size of 50. For the NeoSpectra data, the top-performing model was the RF using raw reflectance spectra, reaching a mean accuracy of 0.9802 and a κ of 0.9719. In contrast, the PSR+ 3500 sensor yielded its best results when using the same classifier but on absorbance spectra processed with SG filters, all yielding the same result of 0.9801 accuracy and 0.9718 κ. At this point, it is worth mentioning that while the tested ML models achieved strong performance, we acknowledge that the degree of separation observed in PCA suggests that simpler classification methods, such as SIMCA, might also perform well in this specific context. Including such a comparison could be a useful direction for future work, particularly for applications where model simplicity is prioritized.

The confusion matrices of the top-performing models for each sensor are illustrated in Fig. 5. For the NeoSpectra sensor (Fig. 5(a)), the RF classifier on reflectance spectra shows minimal misclassifications, with most samples correctly assigned to their respective classes. Similarly, the PSR+ 3500 confusion matrix (Fig. 5(b)) demonstrates high classification performance when using absorbance spectra, confirming the robustness and generalizability of the selected model configurations across sensor types.

To put our results into perspective, our models' performance is compared to the literature, even though most studies focus on quantitative analysis (i.e., regression). (Kar et al., 2017) used a miniaturized StellarNet Inc. spectrometer (900–1700 nm) to detect MY adulteration (1%–25% w/w) in turmeric powder, with the best PLSR model achieved R^2 up to 0.992 and a RMSEP of 0.551. From the reported scatter plot there are a few samples which have errors of more than 5% which could be construed as possible misclassifications, if this was seen from a classification perspective. Rukundo et al. (2020) compared a benchtop and a handheld spectrometer (ASD QualitySpec Trek, 780–2500 nm) for quantifying MY concentrations (0%–30% w/w). Their best PLSR models achieved R^2 values of 0.991 (benchtop) and 0.980 (handheld), with RMSEP of 0.94% and 1.28%, respectively. Their scatter plots show high agreement between predicted and true values, especially at medium to high levels ($\geq$10%), with greater variability at low levels (0%–5%), suggesting reduced reliability for detecting slight adulteration. Lanjewar et al. (2025) proposed an advanced VNIR spectroscopic approach (400–2050 nm, JASCO V-770) combined with spectral pre-processing and ML models to detect MY adulteration in turmeric across a wider concentration range (0.1%–50%). They reported strong predictive accuracy, with R^2 values exceeding 0.99 and classification metrics reaching 97% accuracy. Notably, their benchtop spectrophotometer, although highly sensitive, is inherently restricted to laboratory environments due to its size and operational setup.

In brief, although prior work often employed regression techniques such as PLSR to predict MY content in turmeric, the current study prioritized classification to align with practical field use cases (i.e., binary or categorical quality control decisions). Taken together, these comparisons emphasize that our proposed system bridges the gap between high-performance classification and practical field application. It provides a viable, scalable solution for the non-destructive authentication of turmeric in real-world supply chains, combining the benefits of portability, accuracy, and cost-effectiveness.

An exploratory regression analysis using the same models (RF, XGBoost, SVR) was also conducted and is available in the Supplementary material. While this falls outside the core classification-focused scope of the present study, it may offer additional insight for readers interested in quantitative prediction.

3.2.2. Identification of diagnostic wavelengths through model-driven feature importance analysis

The standardized and interpolated reflectance spectra of all samples acquired with the miniaturized sensor were further examined to identify discrete spectral markers of diagnostic value to enrich the findings of the reflectance spectra and PCA analyses by applying model-driven feature importance metrics presented in Fig. 6.

Feature importances were computed using the best model (i.e., RF on the reflectance spectra), where importance values are estimated based on the mean decrease in impurity—reflecting the average reduction in Gini impurity contributed by each feature across all trees in the ensemble. To obtain a robust representation, importance values were averaged across five cross-validation folds. Subsequently, the most informative spectral regions were identified by applying a peak detection method to the mean importance curve. Peaks were selected based on a minimum height threshold of 0.0075 and a required distance of at least five spectral bands between adjacent peaks, ensuring the isolation of distinct and consistently relevant wavelengths.

The mean feature importance values derived from the optimal model are visualized in Fig. 6(a), highlighting the wavelengths that contributed most significantly to model performance. This approach enables the quantification of the predictive ability of individual wavelengths, leading to the rapid identification of some important peaks in the following spectral regions: 1480–1500 nm, 1640–1680 nm, 1920–2000 nm, 2100–2200 nm, and 2260–2500 nm. Notably, some of these regions overlap with those reported in previous work by (Rukundo et al., 2020), who also identified wavelengths within the 1480–1680 nm, 1740 nm, 2470 nm ranges as critical for diversifying MY from ground turmeric.

Building upon the developed barplot (Fig. 6(a)), the comparison diagram of pure turmeric and MY was generated (Fig. 6(b)), which allowed the exact location in the sensor operating spectrum of the points where the spectral contrast between the two compounds is maximized. The mathematical identification of the spectral points with the highest discriminatory power goes beyond the general spectral trends captured by the continuous profiles in Fig. 3. Thus, while the previous analysis indicated broader spectral bands of interest and the most eye-viewable differentiation peaks among the whole set of samples, the current approach allowed the precise identification of key inflection points, such as at 1495, 1640, 1675, 1885, 1920, 1990, 2035, 2060, 2115, 2155, 2285, 2385, 2440 and 2475 nm.
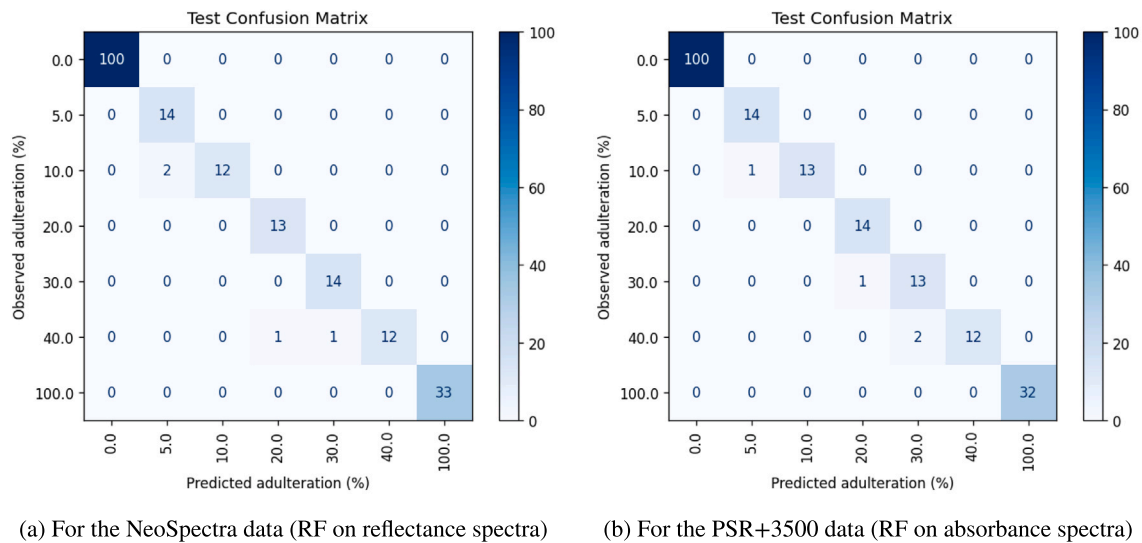
Several of these wavelengths can be linked to specific molecular vibrations characteristic of either turmeric or MY. For instance, the region around 1495 nm corresponds to the first overtone of N–H stretching, commonly associated with the secondary aromatic amine present in MY. Similarly, the spectral region between 1640 nm and 1680 nm is often associated with overtone vibrations of C–H stretching in aromatic systems. While both turmeric (through curcumin) and MY (through multiple substituted phenyl groups) contain aromatic rings, the enhanced spectral importance observed in this region is likely attributed to the unique electronic environment and substitution pattern of the MY molecule, including its sulfonic and azo groups. This explanation is in line with previous spectral studies on MY-containing samples (Dhakal et al., 2016; Rukundo et al., 2020). The broad band from 1920 nm to 2000 nm reflects a combination of O–H stretching and H–O–H bending, relevant to the moisture content (6%–13%) (Nelson et al., 2017) and hydroxyl groups of turmeric (Büning-Pfaue, 2003; Taoheed et al., 2017). Moreover, the peaks at 2115–2155 nm likely reflect a combination of C–H deformation and C=C vibrations, related to curcuminoids found in turmeric. The spectral band around 2140 nm has been reported in turmeric samples and is commonly linked to C–H and C=C stretching vibrations in curcuminoids (Kim et al. 2014). Also, the spectral region between 2285 nm and 2290 nm is attributed to a combination of C–H stretching and $-CH_2$ deformation vibrations, which are commonly observed in polysaccharides such as starch, which is an important part of the turmeric composition (de Macêdo et al., 2021). Finally, the spectral range from 2440 nm to 2475 nm may be potentially ascribed to a combination band from a sharp absorption at 1140 cm^{-1} assigned to MY's characteristic azo C–N stretching and C–H bending vibrations and at 2976 cm^{-1} attributed to C–H stretching (Dhakal et al., 2016).

Table 1

Mean classification accuracy (acc.), Cohen's κ, F1-score, precision, and recall across the five folds, per each learning algorithm and pre-treatment method, for the two different sensors.

Sensor	NeoSpectra Scanner					PSR+ 3500				
	acc.	κ	F1	precision	recall	acc.	κ	F1	precision	recall
Random Forest										
Reflectance	0.98	0.97	0.98	0.99	0.98	0.95	0.93	0.95	0.96	0.95
Reflectance + SNV	0.97	0.95	0.96	0.98	0.97	0.96	0.94	0.95	0.96	0.96
Absorbance + SG1-31	0.97	0.96	0.97	0.98	0.97	0.98	0.97	0.98	0.99	0.98
Absorbance + SG1-51	0.98	0.96	0.97	0.98	0.98	0.98	0.97	0.98	0.99	0.98
Absorbance + SG2-31	0.98	0.96	0.97	0.98	0.98	0.98	0.97	0.98	0.99	0.98
Absorbance + SG2-51	0.98	0.96	0.97	0.98	0.98	0.98	0.97	0.98	0.99	0.98
SVM										
Reflectance	0.98	0.97	0.97	0.98	0.98	0.93	0.89	0.92	0.94	0.93
Reflectance + SNV	0.97	0.95	0.96	0.97	0.97	0.96	0.94	0.95	0.97	0.96
Absorbance + SG1-31	0.98	0.97	0.98	0.99	0.98	0.94	0.92	0.93	0.93	0.94
Absorbance + SG1-51	0.98	0.97	0.98	0.99	0.98	0.96	0.94	0.96	0.97	0.96
Absorbance + SG2-31	0.97	0.95	0.96	0.98	0.97	0.74	0.62	0.72	0.72	0.74
Absorbance + SG2-51	0.97	0.96	0.97	0.98	0.97	0.88	0.82	0.87	0.90	0.88
XGBoost										
Reflectance	0.92	0.88	0.91	0.93	0.92	0.91	0.87	0.91	0.93	0.91
Reflectance + SNV	0.94	0.91	0.93	0.96	0.94	0.94	0.91	0.93	0.95	0.94
Absorbance + SG1-31	0.96	0.94	0.95	0.96	0.96	0.96	0.94	0.96	0.97	0.96
Absorbance + SG1-51	0.94	0.92	0.94	0.95	0.94	0.95	0.93	0.95	0.96	0.95
Absorbance + SG2-31	0.96	0.94	0.96	0.97	0.96	0.94	0.91	0.93	0.94	0.94
Absorbance + SG2-51	0.94	0.91	0.93	0.94	0.94	0.91	0.87	0.91	0.92	0.91

(a) For the NeoSpectra data (RF on reflectance spectra)　　　(b) For the PSR+3500 data (RF on absorbance spectra)

Fig. 5. The confusion matrices of the out-of-fold predictions of the best model.

3.3. Future considerations

Despite the promising classification performance achieved in detecting MY adulteration in pure turmeric using both NeoSpectra and PSR+ 3500 spectral data in conjunction with several state-of-the-art ML classifiers (RF, XGBoost, and SVM), there remains a clear avenue for further research and development. The study was limited to a single adulterant (i.e., MY), which may constrain the generalizability of the models to other common food adulterants. Additionally, the sample size, although sufficient for preliminary analysis, may not capture the full variability present in real-world turmeric adulteration scenarios. Environmental factors including temperature, humidity, and natural lighting also need to be taken into account because they can have an impact on real-time spectral measurements under operational circumstances. To verify real-world dependability, future validation attempts should evaluate the sensor's and models' resilience in such a variety of scenarios. Future work should consider expanding the dataset to include a broader range of adulterants and a more diverse set of turmeric samples from different geographical origins and processing conditions. Moreover, while various spectral pre-treatments were evaluated, model interpretability could be enhanced by developing classifiers that rely solely on the most informative spectral regions identified through feature importance analysis. Such an approach may reduce model complexity and facilitate deployment in portable devices, that further reduce the cost of each sensor. Incorporating additional spectral modalities or extending the study to quantify adulteration levels, rather than only classify them, may also offer valuable insights for future applications. This type of quantitative assessment would, however, require the preparation of a new dataset, as the current one was explicitly constructed by performing weight-to-weight (w/w) mixing and adding the adulterant at predefined concentration levels.

4. Conclusions

This study demonstrated the feasibility of employing a miniaturized FT-NIR spectrometer coupled with Artificial Intelligence (AI)-based classification models, for the real-time detection of turmeric adulteration with Metanil Yellow (MY). The NeoSpectra Scanner (Si-Ware Systems), despite its significantly lower cost and compact form factor, achieved classification performance comparable to that of a high-resolution benchtop VNIR–SWIR spectrometer. Among the tested classifiers, the Random Forest model applied to raw reflectance spectra
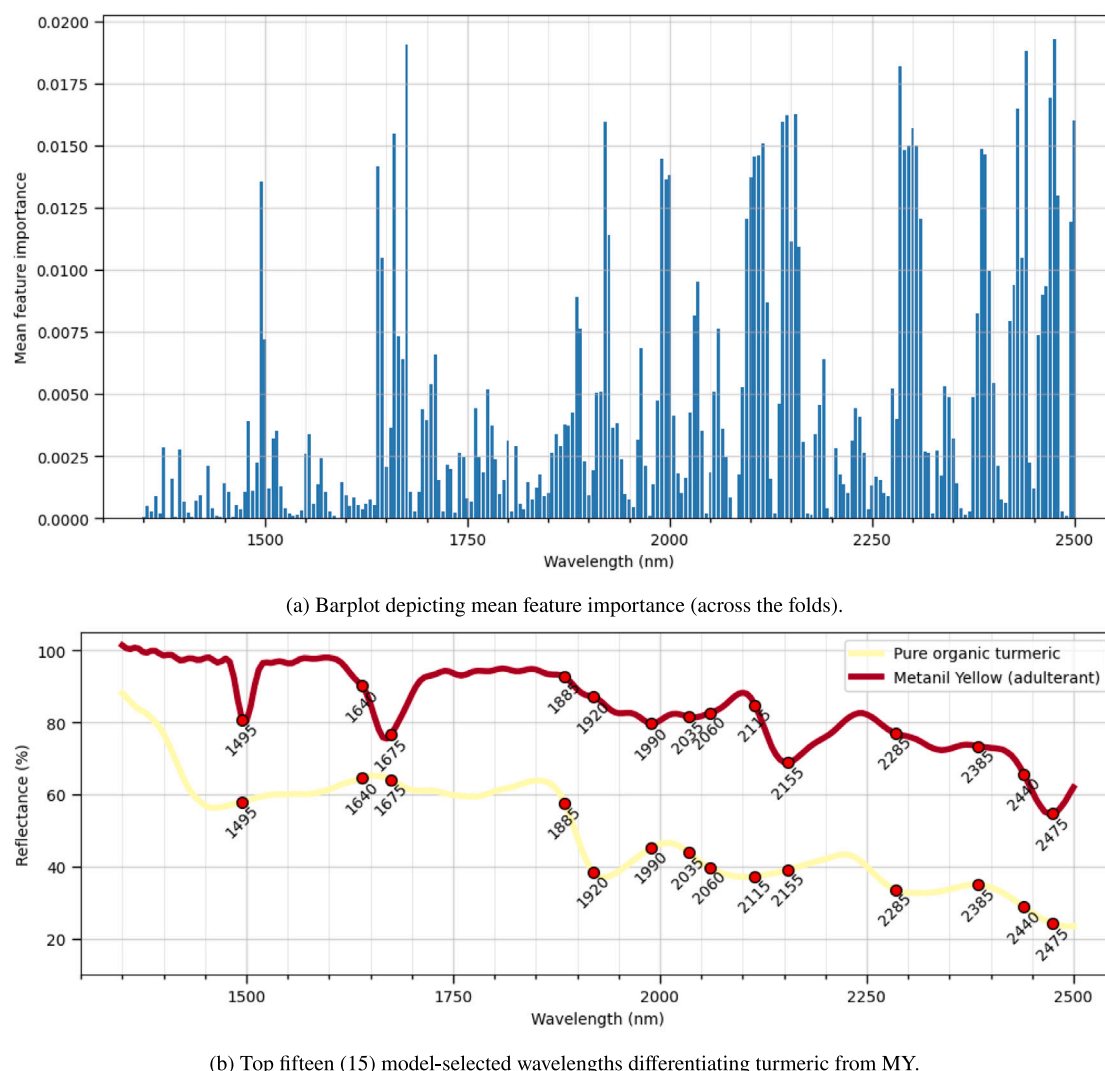
(a) Barplot depicting mean feature importance (across the folds).

(b) Top fifteen (15) model-selected wavelengths differentiating turmeric from MY.

Fig. 6. The most important features (wavelengths) according to the best model for the NeoSpectra sensor: RF model trained on reflectance spectra.

marginally outperformed the others, achieving 98% accuracy and a Cohen's kappa (κ) of 0.97, underscoring the potential of cost-effective portable sensors when paired with robust machine learning techniques.

The use of spectral pre-processing, in combination with model-driven feature importance analysis and nested cross-validation framework, consistently delivered reliable classification outcomes and maintained model transparency. Distinct wavelengths with strong discriminatory capacity, such as 1495 nm, 1640 nm, 1675 nm, 2155 nm, 2475 nm, were pinpointed, aligning with known chemical differences between unadulterated and MY-adulterated turmeric. The practical limit of detection (LOD) was 5% w/w, defined by the lowest tested adulteration level with consistent and accurate classification. These spectral "fingerprints" not only enhance model accuracy but also pave the way for developing faster, simpler, and more affordable sensors. Instead of scanning broad spectral ranges, future devices could focus on just a handful of highly informative bands.

Upcoming research should extend this approach to a more extensive range of adulterants and turmeric varieties or other spices and explore modern methods to further improve its applicability in real-world monitoring contexts. Ultimately, integrating such AI-enhanced NIR systems into accessible digital platforms or apps may empower both industry stakeholders and consumers with reliable, on-site authentication solutions. From a policy perspective, these advancements support broadening access to food safety and quality tools by placing easy-to-use, low-cost technology in the hands of inspectors, producers, and small retailers; potentially reducing dependence from conventional practices and support the transition to a fair, transparent, and sustainable food system.

CRediT authorship contribution statement

Dimitra Xenitopoulou: Writing – original draft, Visualization, Methodology, Investigation, Conceptualization. **Nikolaos L. Tsakiridis:** Writing – original draft, Visualization, Software, Formal analysis, Data curation. **Achilleas Panagiotis Zalidis:** Writing – review & editing, Methodology. **George C. Zalidis:** Supervision, Funding acquisition.

Funding sources

Declaration of competing interest

The authors declare the following financial interests/personal relationships which may be considered as potential competing interests: Dimitra Xenitopoulou reports financial support was provided by Aristotle University of Thessaloniki (Special Account for Research Funds – ELKE). If there are other authors, they declare that they have no known competing financial interests or personal relationships that could have appeared to influence the work reported in this paper.

Appendix A. Supplementary data

Supplementary material related to this article can be found online at https://doi.org/10.1016/j.fufo.2025.100695.

Data availability

The data that support the findings of this study are not publicly available as they are part of the ongoing Horizon Europe project THEROS (Grant Agreement No. 101083579). Data may be available from the corresponding author upon reasonable request and subject to approval by the project consortium and the responsible funding authority.

References

Abd El-Hack, M.E., El-Saadony, M.T., Swelum, A.A., Arif, M., Abo Ghanima, M.M., Shukry, M., Noreldin, A., Taha, A.E., El-Tarabily, K.A., 2021. Curcumin, the active substance of turmeric: its effects on health and ways to improve its bioavailability. J. Sci. Food Agric. 101 (14), 5747–5762. http://dx.doi.org/10.1002/jsfa.11372.

Arabkhani, S., Pourmoslemi, S., Larki Harchegani, A., 2022. Rapid determination of metanil yellow in turmeric using a molecularly imprinted polymer dispersive solid-phase extraction and visible light spectrophotometry. Food Chem. 380, 132120. http://dx.doi.org/10.1016/j.foodchem.2022.132120.

Ashok, V., Agrawal, N., Durgbanshi, A., Esteve-Romero, J., Bose, D., 2015. A novel micellar chromatographic procedure for the determination of metanil yellow in foodstuffs. Anal. Methods 7 (21), 9324–9330. http://dx.doi.org/10.1039/c5ay02377g.

Beć, K.B., Grabska, J., Huck, C.W., 2022. Miniaturized NIR spectroscopy in food analysis and quality control: Promises, challenges, and perspectives. Foods 11 (10), 1465. http://dx.doi.org/10.3390/foods11101465.

Ben Dor, E., Ong, C., Lau, I.C., 2015. Reflectance measurements of soils in the laboratory: Standards and protocols. Geoderma 245–246, 112–124. http://dx.doi.org/10.1016/j.geoderma.2015.01.002.

Bhatkar, N.S., Vimal, Shirkole, S.S., 2023. Future prospect and global market demand for dried herbs, spices and medicinal plants. In: Drying of Herbs, Spices, and Medicinal Plants. CRC Press, pp. 217–229. http://dx.doi.org/10.1201/9781003269250-10.

Bonan, S., Fedrizzi, G., Menotta, S., Elisabetta, C., 2013. Simultaneous determination of synthetic dyes in foodstuffs and beverages by high-performance liquid chromatography coupled with diode-array detector. Dye. Pigment. 99 (1), 36–40. http://dx.doi.org/10.1016/j.dyepig.2013.03.029.

Breiman, L., 2001. Random forests. Mach. Learn. 45 (1), 5–32. http://dx.doi.org/10.1023/a:1010933404324.

Büning-Pfaue, H., 2003. Analysis of water in food by near infrared spectroscopy. Food Chem. 82 (1), 107–115. http://dx.doi.org/10.1016/S0308-8146(02)00583-4.

Buthelezi, N.M.D., Tesfay, S.Z., Ncama, K., Magwaza, L.S., 2019. Destructive and non-destructive techniques used for quality evaluation of nuts: A review. Sci. Hort. 247, 138–146. http://dx.doi.org/10.1016/j.scienta.2018.11.042.

Chen, T., Guestrin, C., 2016. XGBoost: A scalable tree boosting system. In: Proceedings of the 22nd ACM SIGKDD International Conference on Knowledge Discovery and Data Mining. KDD '16, ACM, pp. 785–794. http://dx.doi.org/10.1145/2939672.2939785.

Cortes, C., Vapnik, V., 1995. Support-vector networks. Mach. Learn. 20 (3), 273–297. http://dx.doi.org/10.1007/bf00994018.

Cozzolino, D., 2022. Advantages, opportunities, and challenges of vibrational spectroscopy as tool to monitor sustainable food systems. Food Anal. Methods 15 (5), 1390–1396. http://dx.doi.org/10.1007/s12161-021-02207-w.

de Macêdo, I.Y.L., Machado, F.B., Ramos, G.S., do Carmo Costa, A.G., Batista, R.D., Galvão Filho, A.R., de Souza Gil, E., 2021. Starch adulteration in turmeric samples through multivariate analysis with infrared spectroscopy. Food Chem. 340, 127899. http://dx.doi.org/10.1016/j.foodchem.2020.127899.

Dhakal, S., Chao, K., Schmidt, W., Qin, J., Kim, M., Chan, D., 2016. Evaluation of turmeric powder adulterated with metanil yellow using FT-Raman and FT-IR spectroscopy. Foods 5 (2), 36. http://dx.doi.org/10.3390/foods5020036.

Dixit, S., Khanna, S.K., Das, M., 2008. Asimple 2-directional high-performance thin-layer chromatographic method for the simultaneous determination of curcumin, metanil yellow, and sudan dyes in turmeric, chili, and curry powders. J. AOAC Int. 91 (6), 1387–1396. http://dx.doi.org/10.1093/jaoac/91.6.1387.

Dixit, S., Purshottam, S., Khanna, S., Das, M., 2009. Surveillance of the quality of turmeric powders from city markets of India on the basis of curcumin content and the presence of extraneous colours. Food Addit. Contam.: Part A 26 (9), 1227–1231. http://dx.doi.org/10.1080/02652030903016586.

EFSA Panel on Food Additives, Flavourings, Processing Aids and Materials in Contact with Food (AFC), 2005. Opinion of the scientific panel on food additives, flavourings, processing aids and materials in contact with food (AFC) on a request from the commission related to para hydroxybenzoates (E 214–219). EFSA J. 3 (12), 1–26. http://dx.doi.org/10.2903/j.efsa.2005.263.

El-Saadony, M.T., Yang, T., Korma, S.A., Sitohy, M., Abd El-Mageed, T.A., Selim, S., Al Jaouni, S.K., Salem, H.M., Mahmmod, Y., Soliman, S.M., Mo'men, S.A.A., Mosa, W.F.A., El-Wafai, N.A., Abou-Aly, H.E., Sitohy, B., Abd El-Hack, M.E., El-Tarabily, K.A., Saad, A.M., 2023. Impacts of turmeric and its principal bioactive curcumin on human health: Pharmaceutical, medicinal, and food applications: A comprehensive review. Front. Nutr. 9, http://dx.doi.org/10.3389/fnut.2022.1040259.

Hastie, T., Tibshirani, R., Friedman, J., 2009. The Elements of Statistical Learning. Springer New York, http://dx.doi.org/10.1007/978-0-387-84858-7,

Houhou, R., Bocklitz, T., 2021. Trends in artificial intelligence, machine learning, and chemometrics applied to chemical data. Anal. Sci. Adv. 2 (3–4), 128–141. http://dx.doi.org/10.1002/ansa.202000162.

Islam, S., Jhily, N.J., Parvin, N., Shampad, M.H., Hossain, J., Sarkar, S.C., Rahman, M., Islam, A., 2023. Dreadful practices of adulteration in food items and their worrisome consequences for public health: a review. J. Food Saf. Hyg. http://dx.doi.org/10.18502/jfsh.v8i4.11955.

Jaiswal, S., Yadav, D.S., Mishra, M.K., Gupta, A.K., 2016. Detection of adulterants in spices through chemical method and thin layer chromatography for forensic consideration. Int J Dev Res 6 (08), 8824–8827.

Kalopesa, E., Karyotis, K., Tziolas, N., Tsakiridis, N., Samarinas, N., Zalidis, G., 2023. Estimation of sugar content in wine grapes via in situ VNIR–SWIR point spectroscopy using explainable artificial intelligence techniques. Sensors 23 (3), 1065. http://dx.doi.org/10.3390/s23031065.

Kamali, M., Fazlpour, F., Karimi, F., Rezaee, A., Sadri, F., Hosseini, S.F., 2023. A review of cytotoxic effects of azo dyes on brain-subregion. Middle East J. Rehabil. Heal. Stud. 10 (2), http://dx.doi.org/10.5812/mejrh-130751.

Kar, S., Tudu, B., Bag, A.K., Bandyopadhyay, R., 2017. Application of near-infrared spectroscopy for the detection of metanil yellow in turmeric powder. Food Anal. Methods 11 (5), 1291–1302. http://dx.doi.org/10.1007/s12161-017-1106-9.

Kaur Purba, M., Sudhir K. Shukla, N.A., 2015. Detection of non-permitted food colors in edibles. J. Forensic Res. s4, http://dx.doi.org/10.4172/2157-7145.1000s4-003.

Khan, I.S., Ali, M.N., Hamid, R., Ganie, S.A., 2020. Genotoxic effect of two commonly used food dyes metanil yellow and carmoisine using Allium cepa L. as indicator. Toxicol. Rep. 7, 370–375. http://dx.doi.org/10.1016/j.toxrep.2020.02.009.

Lanjewar, M.G., Morajkar, P.P., Parab, J., 2025. Robust method for detecting metanil yellow in turmeric: Integrating vis-NIR spectroscopy and machine learning. J. Food Comp. Anal. 142, 107409. http://dx.doi.org/10.1016/j.jfca.2024.107409.

Maquet, A., Lievens, A., Paracchini, V., Kaklamanos, G., De La Calle Guntinas, M., Garlant, L., Papoci, S., Pietretti, D., Ždiniaková, T., Breidbach, A., Omar Onaindia, J., Boix Sanfeliu, A., Dimitrova, T., Ulberth, F., 2021. Results of an EU wide coordinated control plan to establish the prevalence of fraudulent practices in the marketing of herbs and spices. Publ. Off. Eur. Union (EUR 30877 EN), http://dx.doi.org/10.2760/309557, JRC126785.

Mukherjee, A., Mandal, B., Banerjee, S., 2009. Turmeric as a carotenoid source on pigmentation and growth of fantail guppy, *Poecilia reticulata*. In: Proceedings of the Zoological Society. 62, Springer-Verlag, pp. 119–123.

Nath, P.P., Sarkar, K., Tarafder, P., Mondal, M., Das, K., Paul, G., 2015. Practice of using metanil yellow as food colour to process food in unorganized sector of west bengal-a case study. Int. Food Res. J. 22 (4), 1424.

Nelson, K.M., Dahlin, J.L., Bisson, J., Graham, J., Pauli, G.F., Walters, M.A., 2017. The essential medicinal chemistry of curcumin: Miniperspective. J. Med. Chem. 60 (5), 1620–1637. http://dx.doi.org/10.1021/acs.jmedchem.6b00975.

Phukan, M., Sahariah, M., Sahu, S., 2022. Study of curcumin content and adulterants present in different marketing brands of turmeric powder. Curr Trends Pharm Res 8 (2), 35–53.

Ranjan, R., Kumar, N., Kiranmayee, A.H., Panchariya, P., 2021. Application of handheld NIR spectroscopy for detection of adulteration in turmeric powder. In: 2021 7th International Conference on Advanced Computing and Communication Systems. ICACCS, IEEE, pp. 1238–1241. http://dx.doi.org/10.1109/icaccs51430.2021.9441790.

Rinnan, Ä., Berg, F.v.d., Engelsen, S.B., 2009. Review of the most common pre-processing techniques for near-infrared spectra. TRAC Trends Anal. Chem. 28 (10), 1201–1222. http://dx.doi.org/10.1016/j.trac.2009.07.007.

Rukundo, I.R., Danao, M.-G.C., 2020. Identifying turmeric powder by source and metanil yellow adulteration levels using near-infrared spectra and PCA-SIMCA modeling. J. Food Prot. 83 (6), 968–974. http://dx.doi.org/10.4315/jfp-19-515.

Rukundo, I.R., Danao, M.-G.C., Weller, C.L., Wehling, R.L., Eskridge, K.M., 2020. Use of a handheld near infrared spectrometer and partial least squares regression to quantify metanil yellow adulteration in turmeric powderf. J. Near Infrared Spectrosc. 28 (2), 81–92. http://dx.doi.org/10.1177/0967033519898889.

Sharifi-Rad, J., Rayess, Y.E., Rizk, A.A., Sadaka, C., Zgheib, R., Zam, W., Sestito, S., Rapposelli, S., Neffe-Skocińska, K., Zielińska, D., Salehi, B., Setzer, W.N., Dosoky, N.S., Taheri, Y., El Beyrouthy, M., Martorell, M., Ostrander, E.A., Suleria, H.A.R., Cho, W.C., Maroyi, A., Martins, N., 2020. Turmeric and its major compound curcumin on health: Bioactive effects and safety profiles for food, pharmaceutical, Biotechnological and medicinal applications. Front. Pharmacol. 11, http://dx.doi.org/10.3389/fphar.2020.01021.

Singletary, K., 2020. Turmeric: Potential health benefits. Nutr. Today 55 (1), 45–56. http://dx.doi.org/10.1097/nt.0000000000000392.

Sultanbawa, Y., Smyth, H., Truong, K., Chapman, J., Cozzolino, D., 2021. Insights on the role of chemometrics and vibrational spectroscopy in fruit metabolite analysis. Food Chem.: Mol. Sci. 3, 100033. http://dx.doi.org/10.1016/j.fochms.2021.100033.

Sundaresan, S., Vijaikanth, V., 2024. Recent advances in electrochemical detection of common azo dyes. Forensic Toxicol. http://dx.doi.org/10.1007/s11419-024-00696-y.

Szymańska, E., 2018. Modern data science for analytical chemical data – a comprehensive review. Anal. Chim. Acta 1028, 1–10. http://dx.doi.org/10.1016/j.aca.2018.05.038.

Szymańska, E., Gerretzen, J., Engel, J., Geurts, B., Blanchet, L., Buydens, L.M., 2015. Chemometrics and qualitative analysis have a vibrant relationship. TRAC Trends Anal. Chem. 69, 34–51. http://dx.doi.org/10.1016/j.trac.2015.02.015.

Taoheed, A.A., Tolulope, A.A., Saidu, A.B., Odewumi, O., Sunday, R.M., Usman, M., 2017. Phytochemical properties, proximate and mineral composition of *curcuma longa* linn. and *zingiber officinale* rosc.: A comparative study. J. Sci. Res. Rep. 13 (4), 1–7.

Tawfeek, S.E., Shalaby, A.M., Alabiad, M.A., Albackoosh, A.-A.A.A., Albakoush, K.M.M., Omira, M.M.A., 2021. Metanil yellow promotes oxidative stress, astrogliosis, and apoptosis in the cerebellar cortex of adult male rat with possible protective effect of scutellarin: A histological and immunohistochemical study. Tissue Cell 73, 101624. http://dx.doi.org/10.1016/j.tice.2021.101624.

Teixeira, A.M., Sousa, C., 2019. A review on the application of vibrational spectroscopy to the chemistry of nuts. Food Chem. 277, 713–724. http://dx.doi.org/10.1016/j.foodchem.2018.11.030.

Verma, A., Saha, S., Bhat, S.K., 2022. Detection of nonpermitted food color metanil yellow in turmeric: A threat to the public health and ayurvedic drug industry. J. Ayurveda 16 (2), 134. http://dx.doi.org/10.4103/joa.joa_77_21.